


Article

Microstructure and Corrosion Resistance of Two-Dimensional TiO₂/MoS₂ Hydrophobic Coating on AZ31B Magnesium Alloy

Longjie Lai ^{1,2}, Heng Wu ^{1,3}, Guobing Mao ^{1,2}, Zhengdao Li ^{4,*}, Li Zhang ⁵ and Qi Liu ^{1,2,*} ¹ School of Materials Science and Engineering, Anhui Polytechnic University, Wuhu 241000, China² Anhui Key Laboratory of High-Performance Non-ferrous Metal Materials, Anhui Polytechnic University, Wuhu 241000, China³ School of Mechanical Engineering, Anhui Institute of Information Technology, Wuhu 241100, China⁴ Chemistry and Pharmaceutical Engineering College, Nanyang Normal University, Nanyang 473061, China⁵ Faculty of Institute of Photoelectronics Thin Film Devices and Technique of Nankai University, Nankai University, Tianjin 300071, China

* Correspondence: nylzd@nynu.edu.cn (Z.L.); modieer_67@ahpu.edu.cn (Q.L.)

Abstract: The corrosion resistance of magnesium alloys can be effectively improved by surface treatment. In this study, a hydrophobic two-dimensional (2D) TiO₂/MoS₂ nanocomposite coating was fabricated on AZ31B magnesium alloy by an electrophoretic deposition method. The corrosion resistance of the coating was evaluated using potentiodynamic polarization and electrochemical impedance spectroscopy analyses. After being modified by a silane coupling agent (KH570), the TiO₂/MoS₂ coating changed from hydrophilic to hydrophobic, and the static water contact angle increased to 131.53°. The corrosion experiment results indicated that the hydrophobic 2D TiO₂/MoS₂ coating had excellent anticorrosion performance (corrosion potential: $E_{\text{corr}} = -0.85 \text{ V}_{\text{Ag}/\text{AgCl}}$, and corrosion current density: $I_{\text{corr}} = 6.73 \times 10^{-8} \text{ A} \cdot \text{cm}^{-2}$). TiO₂/MoS₂ films have promising applications in magnesium alloy corrosion protection.

Keywords: magnesium alloys; electrophoretic deposition; TiO₂/MoS₂; corrosion resistance



Citation: Lai, L.; Wu, H.; Mao, G.; Li, Z.; Zhang, L.; Liu, Q. Microstructure and Corrosion Resistance of Two-Dimensional TiO₂/MoS₂ Hydrophobic Coating on AZ31B Magnesium Alloy. *Coatings* **2022**, *12*, 1488. <https://doi.org/10.3390/coatings12101488>

Academic Editor: Charafeddine Jama

Received: 23 August 2022

Accepted: 1 October 2022

Published: 6 October 2022

Publisher's Note: MDPI stays neutral with regard to jurisdictional claims in published maps and institutional affiliations.



Copyright: © 2022 by the authors. Licensee MDPI, Basel, Switzerland. This article is an open access article distributed under the terms and conditions of the Creative Commons Attribution (CC BY) license (<https://creativecommons.org/licenses/by/4.0/>).

1. Introduction

Magnesium alloys, widely used in the aerospace and automotive industries, have the advantages of high specific strength, low density, good manufacturability and recyclability, and abundant resources [1–4]. However, due to the relatively active chemical properties of magnesium, low standard electrode potential, and poor protection ability of natural oxide film, the corrosion resistance of magnesium alloys is poor [5–7], which limits their wider application. Therefore, improving the corrosion resistance of magnesium alloys can greatly expand their practical application. The commonly used methods to improve the corrosion resistance of magnesium alloys include chemical conversion coating [8], plasma electrolytic oxidation [9], laser surface melting [10], shot peening [11], cold spraying [12], etc. These methods can improve the corrosion resistance of magnesium alloys, but the process is complex, costly, energy-intensive, and poses various environmental issues. On the other hand, constructing a thin film on the surface of magnesium alloys by electrodeposition can effectively slow down the corrosion rate of materials and has the advantages of low cost, convenient operation, rapid film formation, and ease of control [13,14].

Two-dimensional materials have attracted more attention for their potential applications in optics, electrochemical energy storage, biosensing, and other fields due to their special physical properties [15–20]. The 2D materials are also used as coatings to form protective layers, which can act as physical barriers to prevent contact between the corrosive medium and the substrate and avoid corrosion [21,22]. Since graphene was discovered, it has been widely used in the field of corrosion resistance due to its good chemical stability, high strength, and low friction coefficient [23–25]. Single-layer defect-free graphene can

prevent the permeation of molecules. However, defective graphene will accelerate galvanic corrosion [26,27]. In recent years, an increasing number of graphene-like 2D materials have been discovered, such as MoS₂, TiO₂, boron nitride, C₃N₄, and MXene [28–32]. TiO₂ and MoS₂ are two promising two-dimensional materials that have great development potential in the field of anticorrosion. TiO₂ has good chemical and thermal stability. At the same time, due to the lack of interconnected pores in TiO₂, the corrosion resistance of TiO₂ is higher than that of other metal oxides [33–37]. For instance, Devikala et al. [38] showed that with the increase in TiO₂ concentration the corrosion resistance efficiency of composites increased. Rostami et al. [39] demonstrated that the addition of TiO₂ improved the corrosion resistance of the pure cobalt film. Shams Anwar et al. [40] indicated that the addition of TiO₂ nanoparticles improved the corrosion resistance of Zn-Ni alloys. MoS₂ has attracted extensive attention in the field of corrosion protection because of its special (S-Mo-S) three-atomic-layer structure and excellent chemical stability [41,42]. For example, Xia et al. [43] prepared SiO₂ nanoparticles modified by MoS₂ nanosheets, which showed robust corrosion resistance. Hu et al. [44] demonstrated that nano-MoS₂ on a zinc phosphate coating effectively promoted the phosphating process, which improved the corrosion resistance of Q235 low-carbon steel. Chen et al. [45] loaded nano-MoS₂ on the surface of graphene oxide flakes, which endowed the composite coating with excellent barrier properties and significantly improved the corrosion resistance of the coating.

In this work, we describe our recent progress in the synthesis of the hydrophobic nanocomposite coating, which is 2D TiO₂/MoS₂ modified by a silane coupling agent, KH570. This was synthesized to enhance the corrosion resistance of AZ31B magnesium alloy. Because 2D TiO₂ and MoS₂ have similar electronegativity, MoS₂ was added to TiO₂ dispersion to obtain an electrophoretic solution. Then, a TiO₂/MoS₂ thin film was prepared on the surface of the magnesium alloy by electrophoretic deposition. The prepared 2D TiO₂/MoS₂ thin film was modified by KH570. The as-prepared thin film has hydrophobic properties and excellent corrosion resistance, which satisfies the demands of society and has broad application prospects.

2. Materials and Methods

2.1. Materials

AZ31B magnesium alloy (thickness of 1 mm, composition: 2.5–3.5 wt % Al, 0.6–1.4 wt % Zn, 0.2–1.0 wt % Mn, 0.04 wt % Ca, 0.003 wt % Fe, 0.001 wt % Ni, 0.08 wt % Si, 0.01 wt % Cu) was purchased from Dongguan Hongdi Metal Materials Co., Ltd. (Dongguan, China). Silane coupling agent KH570 was purchased from Jinan Xingfeilong Chemical Co., Ltd. (Jinan, China).

2.2. Preparation of TiO₂/MoS₂ Films

The TiO₂ colloid and MoS₂ were synthesized according to previous studies [46,47]. We added 0.7 mL of 1.0 mg/mL MoS₂ aqueous solution to 100 mL of 70% ethanol solution containing 1 mL of TiO₂ colloid. The two magnesium alloy substrates were kept at a distance of 15–20 mm in 5 mL of electrophoresis solution and electrophoresed for 90 s at a constant voltage of 20 V. After electrophoresis, the excess precipitates on the surface were washed with deionized water, dried at room temperature for 48 h, and heated at 150 °C for 60 min to obtain TiO₂/MoS₂ coating.

2.3. Preparation of TiO₂/MoS₂ Films Modified by KH570

The prepared samples were immersed in a beaker containing silane coupling agent, KH570 solution, for 30 min. After repeated rinsing with anhydrous ethanol, the silane-modified TiO₂/MoS₂ surface layer was obtained. The resultant product was denoted as TiO₂/MoS₂-K.

2.4. Analysis of Zeta Potential

The zeta potential of TiO₂ and MoS₂ was determined by Nanometrics (Malvern Zetasizer Nano ZS90, malvernpanalytical). Figure 1 shows the zeta potential diagrams of TiO₂ and MoS₂ measured at 25 °C. The measured electronegativity results are shown in Table 1. On the basis of Figure 1 and Table 1, it is shown that TiO₂ and MoS₂ have similar electronegativity. Therefore, MoS₂ was added to the TiO₂ dispersion, and both were deposited on the anode during electrophoresis deposition.

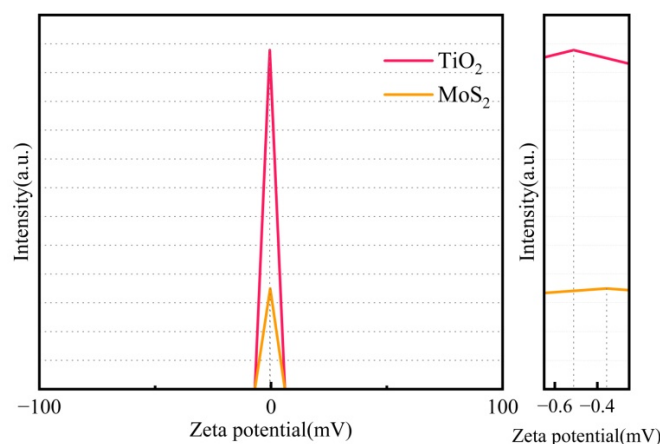


Figure 1. Zeta potential diagram of TiO₂ and MoS₂.

Table 1. Electronegativity of TiO₂ and MoS₂.

Sample	Zeta Potential/mV
TiO ₂	−0.511
MoS ₂	−0.356

2.5. Characteristics of Morphology, Chemical Composition, and Hydrophobic and Anticorrosion Properties

The surface morphology of the samples was observed using an S-4800 scanning electron microscope (SEM, S-4800, Japan Hitachi Corporation, Tokyo, Japan). The phase structure of the samples was characterized by a D-8 X-ray diffractometer (XRD, D8, Beijing Brook Technology Co., Ltd., Beijing, China). The X-ray photoelectron spectroscopy (XPS) analysis was performed using a Thermo ESCALAB 250XI. Fourier transform infrared spectroscopy (FTIR, IRPrestige-21, Shanghai Yixiang Instrument Co., Ltd., Shanghai, China) was carried out for TiO₂/MoS₂ and TiO₂/MoS₂-K. Measurement of the static water contact angle on the sample surface was performed using a contact angle measuring instrument (SDC-100S, Dongguan Shengding Precision Instrument Co., Ltd., Dongguan, China); 6 µL was set as the drip volume in the test, and multiple measurements were performed at different positions on the surface of each sample, with the average value of multiple measurements taken for analysis. Metal corrosion in the atmosphere was simulated by a salt spray corrosion test box (DF-YWX/Q-150, Nanjing Defu Test Equipment Co., Ltd., Nanjing, China); 5 wt % NaCl solution was prepared as the test solution. The experimental temperature was controlled at 35 ± 2 °C, and the pressure of the atomized salt solution was maintained in the range of 69~172 kPa. The sample size was 10 × 10 × 1 mm. An electrochemical workstation (CHI760E, Shanghai Chenhua, Shanghai, China) was used to test the corrosion polarization curve of the magnesium alloy samples. A 3.5% NaCl solution was used as the electrolyte, and a three-electrode system was adopted, in which AgCl was used as the reference electrode and Pt was used as the counter electrode, and the scanning speed was 5 mV/s. The determination of E_{corr} is the abscissa corresponding to

the intersection of the cathode zone and the anode zone, and I_{cor} is the intersection of the tangent of the cathode zone and the vertical line corresponding to E_{cor} .

3. Results and Discussion

3.1. Morphology Analysis of $\text{TiO}_2/\text{MoS}_2$ Films

The surface morphology of the films deposited on the magnesium alloy substrate at different magnifications is presented in Figure 2. According to Figure 2a,b, a layer of a fog-like film composed of nanosheets is evenly spread on the surface of AZ31B. The bright white point is due to the tiny residual particles of titanate when it is exfoliated into TiO_2 . In Figure 2c,d, the cracks are clearly displayed, which are caused by the accumulation of large amounts of MoS_2 in the substrate surface solution during electrophoretic deposition. Figure 2d shows the microscopic magnification of the relatively flat area. The nanosheets are stacked together to form large particles. The surface roughness was increased, and obvious cracks could be observed. As shown in Figure 2e, the surface layer completely and uniformly covers the surface of AZ31B, and there is no honeycomb connection between the nanosheets, which becomes very dense. The contact between the surface of AZ31B and air or corrosive substances is completely isolated, and a good protective barrier is formed [48,49]. Figure 2f shows that the coating becomes denser after KH570 modification.

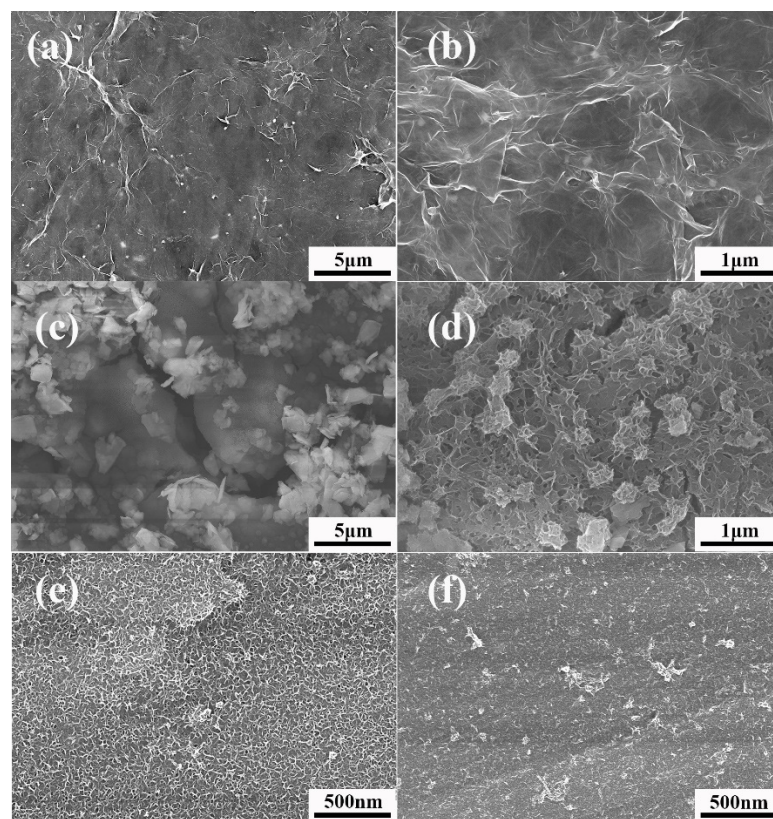


Figure 2. SEM images of films deposited on AZ31B: (a,b) TiO_2 , (c,d) MoS_2 , (e) $\text{TiO}_2/\text{MoS}_2$, (f) $\text{TiO}_2/\text{MoS}_2\text{-K}$.

3.2. Compositional Analysis of $\text{TiO}_2/\text{MoS}_2$ Films

Figure 3 shows the XRD patterns of the AZ31B substrate, TiO_2 and MoS_2 powder and $\text{TiO}_2/\text{MoS}_2$ film. The difference in peak position represents the difference in TiO_2 layer spacing, which proves that TiO_2 with random layer spacing is prepared [50,51]. The peaks of MoS_2 powder correspond to the hexagonal MoS_2 standard card (JCPDS No. 37-1492). Notably, after preparing $\text{TiO}_2/\text{MoS}_2$ film on the surface of the magnesium alloy, the peaks of TiO_2 and MoS_2 are not obvious due to the strong peak of the AZ31B substrate. Combined

with the results of the energy spectrum analysis of the corrosion products of the samples, $\text{TiO}_2/\text{MoS}_2$ films were successfully prepared.

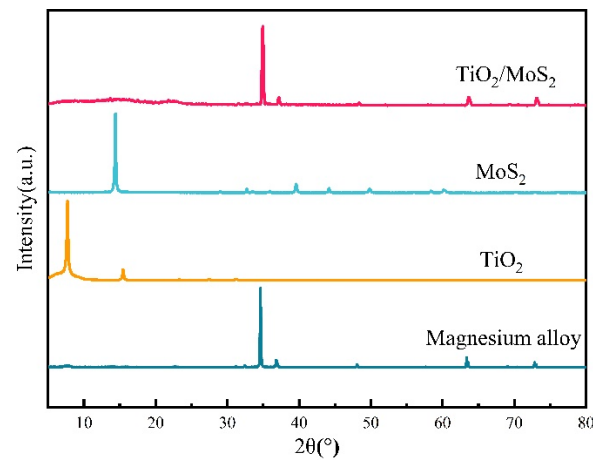


Figure 3. XRD patterns of magnesium alloy, TiO_2 , MoS_2 , and $\text{TiO}_2/\text{MoS}_2$ films.

3.3. XPS of $\text{TiO}_2/\text{MoS}_2$ Coating

XPS measurements were conducted to characterize the surface compositions. As shown in Figure 4, TiO_2 features two characteristic peaks at around 463.9 and 458.2 eV, corresponding to the $\text{Ti } 2p^{1/2}$ and $\text{Ti } 2p^{3/2}$ components, respectively. In Figure 4c, two peaks at 233.1 and 229.9 eV are assigned to $\text{Mo } 3d^{3/2}$ and $\text{Mo } 3d^{5/2}$, which suggests that the majority of Mo at the surface is Mo^{4+} . Simultaneously, the peak at 227.1 eV belongs to the S 2s orbital of MoS_2 . The S 2p XPS spectrum shows that two peaks located at 163.9 and 162.9 eV correspond to $\text{S } 2p^{1/2}$ and $\text{S } 2p^{3/2}$, which is consistent with the -2 oxidation state of sulfur. This confirms the successful synthesis of $\text{TiO}_2/\text{MoS}_2$.

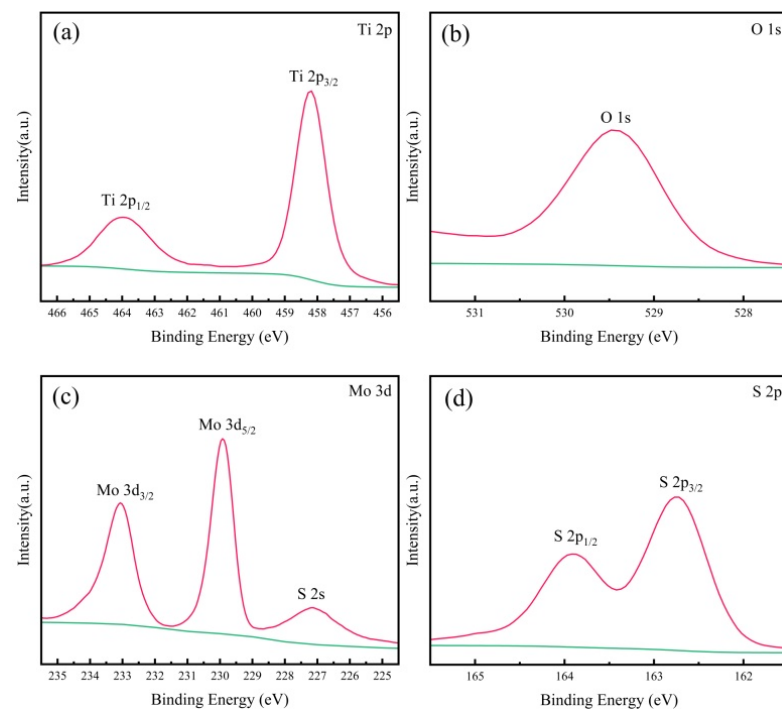


Figure 4. XPS spectra of $\text{TiO}_2/\text{MoS}_2$: (a) Ti 2p, (b) O 1s, (c) Mo 3d, (d) S 2p.

3.4. Hydrophilicity Test of TiO₂/MoS₂ Films

The wettability of the material surface also has an important influence on the corrosion resistance of the material. It is generally believed that the hydrophobic surface makes it more difficult for water molecules or chloride ions to penetrate the metal surface due to the isolation effect, thereby inhibiting the corrosion of the metal [52–54]. The contact angles (CA) of the magnesium alloy and the TiO₂/MoS₂ and TiO₂/MoS₂-K films are presented in Figure 5a. As shown in Figure 5a, the CA of the magnesium alloy is 36.08°, indicating that the surface of the AZ31B substrate without coatings is hydrophilic. When the TiO₂/MoS₂ surface layer was electrophoretically deposited on the surface of the AZ31B substrate, the CA increased to 65.43°. When the TiO₂/MoS₂ film was modified by KH570, the CA value was 131.53°. Another important observation is that the surface of the alloy changes from hydrophilic to hydrophobic. This is because the silane coupling agent KH570 is hydrolyzed into silanol in the solution, and the silanol is condensed with -OH on the TiO₂/MoS₂ film [55]. The hydrophilic functional group (-OH) of the TiO₂/MoS₂ coating was replaced by the organic functional group in silanol, and the reaction process is shown in Formulas (1)–(3). Figure 5b shows the FTIR spectra of TiO₂/MoS₂ and TiO₂/MoS₂-K. Two new peaks of TiO₂/MoS₂-K at about 1240 and 1280 cm⁻¹ are attributed to stretching vibrations of C-O-C. Meanwhile, the absorption peak at 1710 cm⁻¹ is assigned to the stretching vibration of C=O. The intensity of TiO₂/MoS₂-K is weaker than that of TiO₂/MoS₂ because the organic functional groups in silanol replace -OH on the surface of silane-modified TiO₂/MoS₂. These results indicate that the surface of the TiO₂/MoS₂ surface layer is modified by KH570, thereby enhancing the surface hydrophobicity of TiO₂/MoS₂ [56]. This effectively isolates the magnesium alloy from making contact with liquid, making it more difficult for water molecules or chloride ions to penetrate the metal surface and effectively enhancing the corrosion resistance of the magnesium alloy [57].

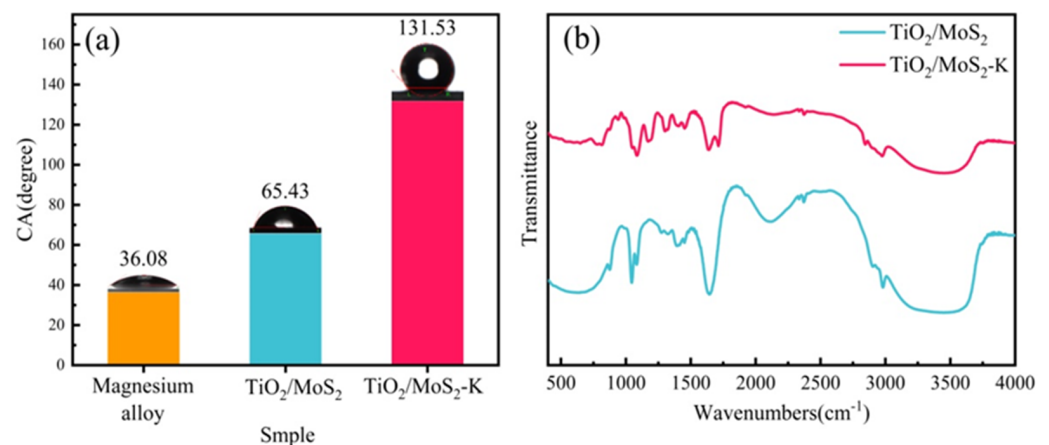
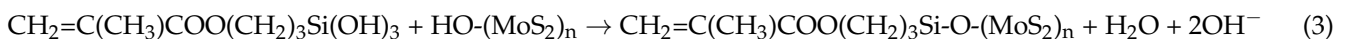
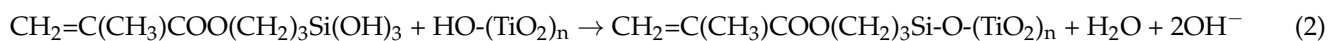
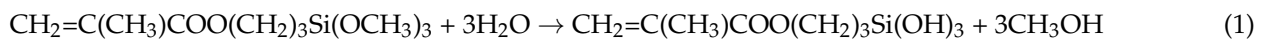


Figure 5. (a) Contact angles of magnesium alloy, TiO₂/MoS₂, and TiO₂/MoS₂-K; (b) FT-IR spectra of TiO₂/MoS₂ and TiO₂/MoS₂-K.

3.5. Electrochemical Test of TiO₂/MoS₂ Films

Figure 6 shows the potentiodynamic polarization curves of all the samples in 3.5 wt % NaCl aqueous solution. The results of the test are summarized in Table 2. On the basis of Figure 6 and Table 2, it is shown that the corrosion current density (I_{corr}) of the magnesium alloy decreases after electrophoresis. The polarization curve shape of the sample after deposition is similar to that of the magnesium alloy substrate, indicating that the 2D films

do not change the corrosion kinetics process of the magnesium alloy. The contact between the substrate and the corrosion medium is isolated by the surface thin film, which improves the corrosion resistance of the magnesium alloy to a certain extent. The corrosion potential (E_{corr}) of the AZ31B magnesium alloy is -1.47 V and the I_{corr} is $6.81 \times 10^{-4} \text{ A}\cdot\text{cm}^{-2}$, indicating that the corrosion resistance of the magnesium alloy matrix is poor [58]. The results show that the E_{corr} of $\text{TiO}_2/\text{MoS}_2\text{-K}$ has a higher potential compared with TiO_2 , MoS_2 , and $\text{TiO}_2/\text{MoS}_2$ composite coatings. Among them, $\text{TiO}_2/\text{MoS}_2\text{-K}$ has the lowest I_{corr} . The I_{corr} values for the TiO_2 and MoS_2 surface layer are 5.13×10^{-6} and $2.19 \times 10^{-5} \text{ A}\cdot\text{cm}^{-2}$, respectively, whereas that of the $\text{TiO}_2/\text{MoS}_2$ film is $3.69 \times 10^{-7} \text{ A}\cdot\text{cm}^{-2}$. The I_{corr} of the $\text{TiO}_2/\text{MoS}_2$ film decreases by two orders of magnitude compared to the MoS_2 film, which is due to the dense state of the $\text{TiO}_2/\text{MoS}_2$ coating. The E_{corr} of the $\text{TiO}_2/\text{MoS}_2\text{-K}$ film is -0.85 V, and the I_{corr} is $6.73 \times 10^{-8} \text{ A}\cdot\text{cm}^{-2}$. Compared with the $\text{TiO}_2/\text{MoS}_2$ film, the E_{corr} of the $\text{TiO}_2/\text{MoS}_2\text{-K}$ film shifted positively by 0.15 V, and the I_{corr} decreased by six times. This indicates that the KH570 modification improved the corrosion resistance of the $\text{TiO}_2/\text{MoS}_2$ protective layer, which is ascribed to its effectively isolating the magnesium alloy from contacting the corrosive liquid.

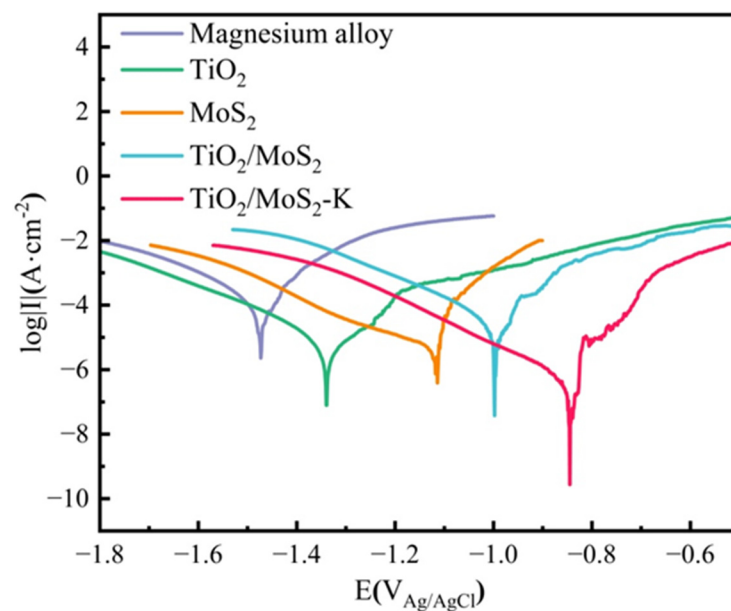


Figure 6. Polarization curves of magnesium alloy, TiO_2 , MoS_2 , $\text{TiO}_2/\text{MoS}_2$, $\text{TiO}_2/\text{MoS}_2\text{-K}$.

Table 2. Potentiodynamic polarization curves of samples in 3.5 wt % NaCl aqueous solution.

Sample	$E_{\text{corr}}/(\text{V}_{\text{Ag/AgCl}})$	$I_{\text{corr}}/(\text{A}\cdot\text{cm}^{-2})$
Magnesium alloy	-1.47	6.81×10^{-4}
TiO_2	-1.34	5.13×10^{-6}
MoS_2	-1.11	2.19×10^{-5}
$\text{TiO}_2/\text{MoS}_2$	-1.00	3.69×10^{-7}
$\text{TiO}_2/\text{MoS}_2\text{-K}$	-0.85	6.73×10^{-8}

To further characterize corrosion resistance, we used EIS to analyze the anticorrosion of the sample. Figure 7 shows the electrochemical impedance spectroscopy of magnesium alloy, TiO_2 , $\text{TiO}_2/\text{MoS}_2\text{-K}$. The electrochemical impedance spectroscopy data are described in detail by the numerical fitting of experimental data. The corresponding equivalent circuit was selected to fit the impedance data, as shown in Figure 8. The fitting circuit of the magnesium alloy substrate is shown in Figure 8a, and the fitting circuit of the samples with TiO_2 film and those with $\text{TiO}_2/\text{MoS}_2\text{-K}$ films is shown in Figure 8b [59]. The results are shown in Table 3. The circuit involves the solution resistance (R_s), the charge transfer

resistance (R_{ct}) of the Mg particles, and the electric double-layer capacitance (CPE_{dl}) at the interface between the electrolyte and magnesium particles. R_p is the inductance resistance, and CPL_{film} is the inductance, corresponding to the electrode reaction between the film layer and the electrolyte interface. It is reported that R_{ct} is closely related to the corrosion process, that is, the higher the R_{ct} , the better the corrosion resistance. It can be seen from the results that the impedance radius of the TiO_2/MoS_2-K sample is the largest, and the R_{ct} value is the largest at $871.9 \Omega \cdot cm^2$, which is significantly higher than that of the magnesium alloy sample and the sample with the TiO_2 film. It shows that the corrosion resistance of TiO_2/MoS_2-K is the highest, which is consistent with the results of the polarization curve.

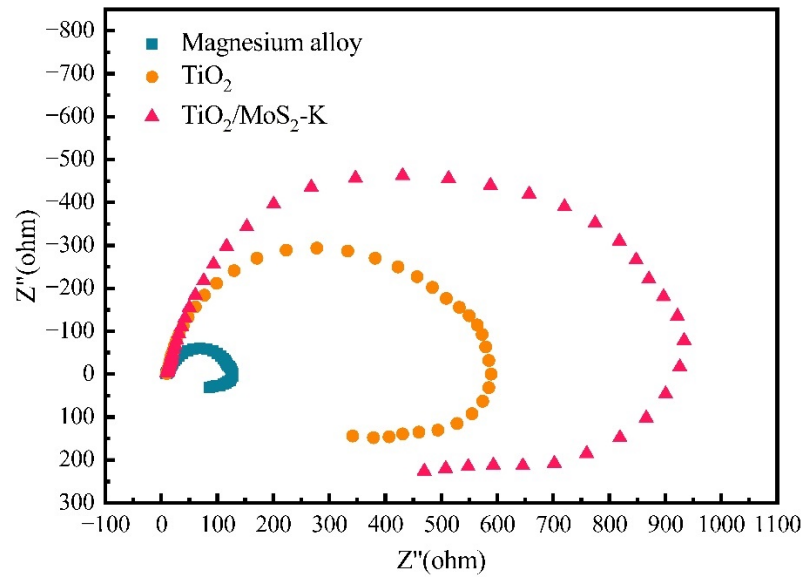


Figure 7. Electrochemical impedance spectroscopy of magnesium alloy, TiO_2 , TiO_2/MoS_2-K .

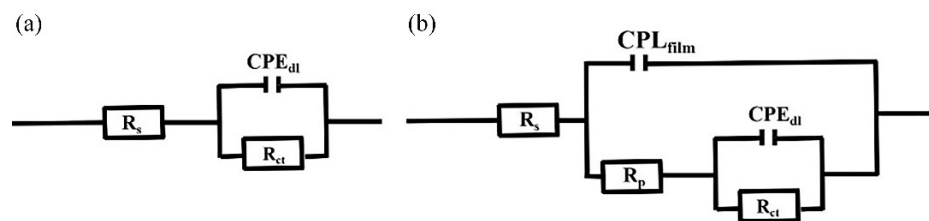


Figure 8. Equivalent circuits for EIS spectra: (a) magnesium alloy, (b) TiO_2 thin film and TiO_2/MoS_2-K thin film.

Table 3. Electrochemical data extracted from ECs fitting of the EIS curves.

Sample	R_s ($\Omega \cdot cm^2$)	CPE_{film} (F/cm^2)	R_p ($\Omega \cdot cm^2$)	CPE_{dl-T} (F/cm^2)	CPE_{dl-P} (F/cm^2)	R_{ct} ($\Omega \cdot cm^2$)
Magnesium alloy	10.2	-	-	7.11×10^{-6}	-	111.9
TiO_2	8.97	1.27×10^{-6}	16.96	1.66×10^{-6}	0.98	659.6
TiO_2/MoS_2-K	9.25	8.92×10^{-6}	19.29	1.87×10^{-6}	0.95	871.9

3.6. Salt Spray Corrosion Experiment of TiO_2/MoS_2 Films

Figure 9 shows the comparison of the surface morphology of the magnesium alloy samples, electrophoretically deposited TiO_2 , and TiO_2/MoS_2-K after the neutral salt spray test for 24, 48, and 72 h. Table 4 shows the results of the energy spectrum analysis of the corrosion products of the samples. It can be seen from the data in Table 4 that, in addition to the original elements, Na and Cl elements were also added to all the corrosion products

of the samples, indicating that the chemical corrosion process occurred in the samples and salt spray. Combined with the SEM images, it can be seen that pitting corrosion occurred on the samples with $\text{TiO}_2/\text{MoS}_2\text{-K}$ film, which is similar to that on the samples with TiO_2 coating. With increasing time, the corrosion area increased gradually, but it was smaller than that on the surface of the magnesium alloy and the samples with the TiO_2 layer. This was mainly due to the good chemical stability of TiO_2 and MoS_2 and the formation of the dense protective layer after electrophoresis. The hydrophobic thin film modified by KH570 further delayed the corrosion of the magnesium alloy.

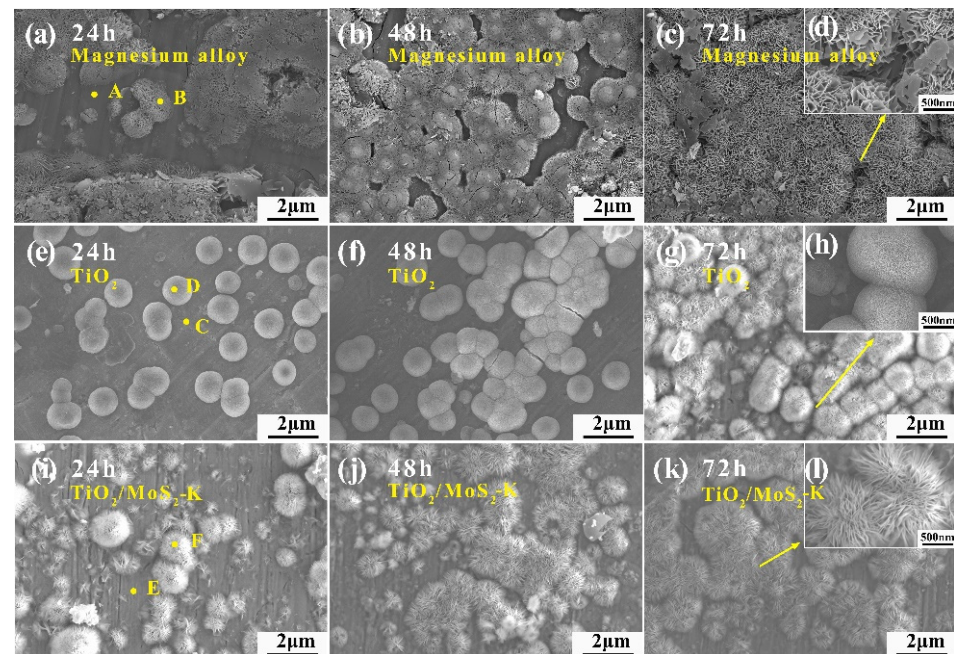


Figure 9. The microstructure of the sample surface after salt spray test at different times. Magnesium alloy: (a) 24 h, (b) 48 h, (c) 72 h; TiO_2 film: (e) 24 h, (f) 48 h, (g) 72 h; $\text{TiO}_2/\text{MoS}_2\text{-K}$ film: (i) 24 h, (j) 48 h, (k) 72 h. The (d,h,l) insets are partial enlargements of (c,g,k), respectively.

Table 4. Energy spectrum analysis of neutral salt spray test products (at. %).

Point	O	Mg	Mn	Ti	Na	Cl	Mo	S
A	57.64	26.18	12.02	0	2.79	1.37	0	0
B	59.23	25.43	11.08	0	2.51	1.75	0	0
C	55.38	25.28	12.60	2.40	3.15	1.19	0	0
D	53.85	25.32	11.06	3.99	3.98	1.80	0	0
E	55.62	25.16	11.10	3.69	2.17	1.12	0.22	0.92
F	56.38	25.09	11.20	2.57	2.23	1.33	0.19	1.01

Figure 10 shows the salt spray corrosion weight gain of the magnesium alloy samples after electrophoretic deposition of TiO_2 and $\text{TiO}_2/\text{MoS}_2\text{-K}$ films. The weight gain rate of the sample with $\text{TiO}_2/\text{MoS}_2\text{-K}$ is higher at the beginning of the test than that of the magnesium alloy sample and the sample with TiO_2 coating. With increasing salt spray corrosion time, the weight gain rate of the sample gradually slows down because the corrosion products on the surface of the sample increase, which hinders the continuous reaction of chloride ion contact with the magnesium alloy surface. In addition, the weight gain of the sample with the $\text{TiO}_2/\text{MoS}_2\text{-K}$ film is significantly lower than that of the former two samples, and the corrosion rate is the lowest. This result indicates that the $\text{TiO}_2/\text{MoS}_2\text{-K}$ protective layer delayed the corrosion of the magnesium alloy to a greater extent and had the best corrosion resistance.

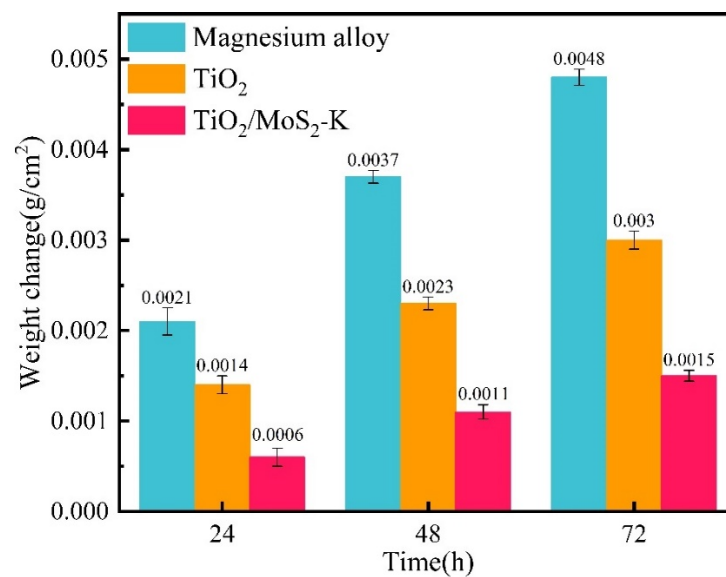


Figure 10. Salt spray corrosion weight gain diagram.

4. Conclusions

The TiO₂/MoS₂ coating was successfully prepared on the surface of the magnesium alloy by adding MoS₂ in the electrophoretic deposition of TiO₂. After the TiO₂/MoS₂ layer was modified by the silane coupling agent KH570, the wettability of the magnesium alloy surface was changed from hydrophilic to hydrophobic. The as-prepared TiO₂/MoS₂-K film had a contact angle of 131.53°. Combined with the electrochemical test and salt spray corrosion analysis, it can be seen that the TiO₂/MoS₂-K film developed a significantly improved anticorrosion property compared to the magnesium alloy. In addition, we anticipate a promising potential to transfer this technology to other metal substrates for important applications.

Author Contributions: Conceptualization, Q.L. and Z.L.; methodology, H.W.; investigation, L.L.; writing-original draft preparation, L.L.; writing-review and editing, G.M.; supervision, Q.L.; project administration, L.Z.; funding acquisition, Q.L. All authors have read and agreed to the published version of the manuscript.

Funding: This work was supported by the Natural Science Foundation of Anhui Province (No. 2008085ME132) and the Key Project of Anhui Provincial Department of Education (No. KJ2019A0157).

Conflicts of Interest: The authors declare no conflict of interest.

References

- Luo, K.; Zhang, L.; Wu, G.; Liu, W.; Ding, W. Effect of Y and Gd content on the microstructure and mechanical properties of Mg–Y–RE alloys. *J. Magnes. Alloy.* **2019**, *7*, 345–354. [[CrossRef](#)]
- Yang, Y.; Xiong, X.; Chen, J.; Peng, X.; Chen, D.; Pan, F. Research advances in magnesium and magnesium alloys worldwide in 2020. *J. Magnes. Alloy.* **2021**, *9*, 705–747. [[CrossRef](#)]
- Liu, H.; Tong, Z.; Yang, Y.; Zhou, W.; Chen, J.; Pan, X.; Ren, X. Preparation of phosphate conversion coating on laser surface textured surface to improve corrosion performance of magnesium alloy. *J. Alloys Compd.* **2021**, *865*, 158701. [[CrossRef](#)]
- Xianhua, C.; Yuxiao, G.; Fusheng, P. Research Progress in Magnesium Alloys as Functional Materials. *Rare Met. Mater. Eng.* **2016**, *45*, 2269–2274. [[CrossRef](#)]
- Song, J.; She, J.; Chen, D.; Pan, F. Latest research advances on magnesium and magnesium alloys worldwide. *J. Magnes. Alloy.* **2020**, *8*, 1–41. [[CrossRef](#)]
- Siddique, S.; Bernussi, A.A.; Husain, S.W.; Yasir, M. Enhancing structural integrity, corrosion resistance and wear properties of Mg alloy by heat treated cold sprayed Al coating. *Surf. Coat. Technol.* **2020**, *394*, 125882. [[CrossRef](#)]
- Yeganeh, M.; Mohammadi, N. Superhydrophobic surface of Mg alloys: A review. *J. Magnes. Alloy.* **2018**, *6*, 59–70. [[CrossRef](#)]
- Chang, S.-H.; Niu, L.; Su, Y.; Wang, W.; Tong, X.; Li, G. Effect of the pretreatment of silicone penetrant on the performance of the chromium-free chemfilm coated on AZ91D magnesium alloys. *Mater. Chem. Phys.* **2016**, *171*, 312–317. [[CrossRef](#)]

9. Ballam, L.R.; Arab, H.; Bestetti, M.; Franz, S.; Masi, G.; Sola, R.; Donati, L.; Martini, C. Improving the Corrosion Resistance of Wrought ZM21 Magnesium Alloys by Plasma Electrolytic Oxidation and Powder Coating. *Materials* **2021**, *14*, 2268. [[CrossRef](#)]
10. Liu, C.; Liang, J.; Zhou, J.; Wang, L.; Li, Q. Effect of laser surface melting on microstructure and corrosion characteristics of AM60B magnesium alloy. *Appl. Surf. Sci.* **2015**, *343*, 133–140. [[CrossRef](#)]
11. Lu, F.-F.; Ma, K.; Li, C.-X.; Yasir, M.; Luo, X.-T.; Li, C.-J. Enhanced corrosion resistance of cold-sprayed and shot-peened aluminum coatings on LA43M magnesium alloy. *Surf. Coat. Technol.* **2020**, *394*, 125865. [[CrossRef](#)]
12. Yao, H.-L.; Yi, Z.-H.; Yao, C.; Zhang, M.-X.; Wang, H.-T.; Li, S.-B.; Bai, X.-B.; Chen, Q.-Y.; Ji, G.-C. Improved corrosion resistance of AZ91D magnesium alloy coated by novel cold-sprayed Zn-HA/Zn double-layer coatings. *Ceram. Int.* **2020**, *46*, 7687–7693. [[CrossRef](#)]
13. Hosseini, M.R.; Ahangari, M.; Johar, M.H.; Allahkaram, S.R. Optimization of nano HA-SiC coating on AISI 316L medical grade stainless steel via electrophoretic deposition. *Mater. Lett.* **2021**, *285*, 129097. [[CrossRef](#)]
14. Guan, S.; Hao, L.; Yoshida, H.; Itoi, T.; Cheng, Y.; Seki, S.; Nishina, Y.; Lu, Y. Enhanced photocatalytic activity and stability of TiO₂/graphene oxide composites coatings by electrophoresis deposition. *Mater. Lett.* **2021**, *286*, 129258. [[CrossRef](#)]
15. Sun, T.-Y.; Hao, Y.; Wu, Y.-H.; Zhao, W.-J.; Huang, L.-F. Corrosion Resistance of Ultrathin Two-Dimensional Coatings: First-Principles Calculations towards In-Depth Mechanism Understanding and Precise Material Design. *Metals* **2021**, *11*, 2011. [[CrossRef](#)]
16. Mak, K.F.; Shan, J. Photonics and optoelectronics of 2D semiconductor transition metal dichalcogenides. *Nat. Photonics* **2016**, *10*, 216–226. [[CrossRef](#)]
17. Lu, Q.; Yu, Y.; Ma, Q.; Chen, B.; Zhang, H. 2D Transition-Metal-Dichalcogenide-Nanosheet-Based Composites for Photocatalytic and Electrocatalytic Hydrogen Evolution Reactions. *Adv. Mater.* **2016**, *28*, 1917–1933. [[CrossRef](#)] [[PubMed](#)]
18. Kumar, K.S.; Choudhary, N.; Jung, Y.; Thomas, J. Recent Advances in Two-Dimensional Nanomaterials for Supercapacitor Electrode Applications. *ACS Energy Lett.* **2018**, *3*, 482–495. [[CrossRef](#)]
19. Choi, W.; Choudhary, N.; Han, G.H.; Park, J.; Akinwande, D.; Lee, Y.H. Recent development of two-dimensional transition metal dichalcogenides and their applications. *Mater. Today* **2017**, *20*, 116–130. [[CrossRef](#)]
20. Bhandavat, R.; David, L.; Singh, G. Synthesis of Surface-Functionalized WS₂ Nanosheets and Performance as Li-Ion Battery Anodes. *J. Phys. Chem. Lett.* **2012**, *3*, 1523–1530. [[CrossRef](#)]
21. Ding, R.; Chen, S.; Lv, J.; Zhang, W.; Zhao, X.-d.; Liu, J.; Wang, X.; Gui, T.-J.; Li, B.-J.; Tang, Y.-Z.; et al. Study on graphene modified organic anti-corrosion coatings: A comprehensive review. *J. Alloys Compd.* **2019**, *806*, 611–635. [[CrossRef](#)]
22. Seel, M.; Pandey, R. Proton and hydrogen transport through two-dimensional monolayers. *2D Mater.* **2016**, *3*, 025004. [[CrossRef](#)]
23. Prasai, D.; Tuberquia, J.C.; Harl, R.R.; Jennings, G.K.; Bolotin, K.I. Graphene: Corrosion-inhibiting coating. *ACS Nano* **2012**, *6*, 1102–1108. [[CrossRef](#)] [[PubMed](#)]
24. Zhao, Z.; Hou, T.; Wu, N.; Jiao, S.; Zhou, K.; Yin, J.; Suk, J.W.; Cui, X.; Zhang, M.; Li, S.; et al. Polycrystalline Few-Layer Graphene as a Durable Anticorrosion Film for Copper. *Nano Lett.* **2021**, *21*, 1161–1168. [[CrossRef](#)] [[PubMed](#)]
25. Bohm, S. Graphene against corrosion. *Nat. Nanotechnol.* **2014**, *9*, 741–742. [[CrossRef](#)] [[PubMed](#)]
26. Cui, C.; Lim, A.T.O.; Huang, J. A cautionary note on graphene anti-corrosion coatings. *Nat. Nanotechnol.* **2017**, *12*, 834–835. [[CrossRef](#)] [[PubMed](#)]
27. Zhang, Y.; Sun, J.; Xiao, X.; Wang, N.; Meng, G.; Gu, L. Graphene-like two-dimensional nanosheets-based anticorrosive coatings: A review. *J. Mater. Sci. Technol.* **2022**, *129*, 139–162. [[CrossRef](#)]
28. Nurdiwijayanto, L.; Nishijima, H.; Miyake, Y.; Sakai, N.; Osada, M.; Sasaki, T.; Taniguchi, T. Solution-Processed Two-Dimensional Metal Oxide Anticorrosion Nanocoating. *Nano Lett.* **2021**, *21*, 7044–7049. [[CrossRef](#)]
29. Shi, K.; Meng, X.; Xiao, S.; Chen, G.; Wu, H.; Zhou, C.; Jiang, S.; Chu, P.K. MXene Coatings: Novel Hydrogen Permeation Barriers for Pipe Steels. *Nanomaterials* **2021**, *11*, 2737. [[CrossRef](#)]
30. Mujib, S.B.; Mukherjee, S.; Ren, Z.; Singh, G. Assessing corrosion resistance of two-dimensional nanomaterial-based coatings on stainless steel substrates. *R. Soc. Open Sci.* **2020**, *7*, 200214. [[CrossRef](#)]
31. Shen, L.; Zhao, W.; Wang, K.; Xu, J. GO-Ti₃C₂ two-dimensional heterojunction nanomaterial for anticorrosion enhancement of epoxy zinc-rich coatings. *J. Hazard. Mater.* **2021**, *417*, 126048. [[CrossRef](#)] [[PubMed](#)]
32. Xi, K.; Wu, H.; Zhou, C.; Qi, Z.; Yang, K.; Fu, R.K.Y.; Xiao, S.; Wu, G.; Ding, K.; Chen, G.; et al. Improved corrosion and wear resistance of micro-arc oxidation coatings on the 2024 aluminum alloy by incorporation of quasi-two-dimensional sericite microplates. *Appl. Surf. Sci.* **2022**, *585*, 152693. [[CrossRef](#)]
33. Wang, X. Preparation and Corrosion Resistance of AKT-Waterborne Polyurethane Coating. *Int. J. Electrochem. Sci.* **2020**, *15*, 1450–1464. [[CrossRef](#)]
34. Kavimani, V.; Prakash, K.S.; Gunashri, R.; Sathish, P. Corrosion protection behaviour of r-GO/TiO₂ hybrid composite coating on Magnesium substrate in 3.5 wt.% NaCl. *Prog. Org. Coat.* **2018**, *125*, 358–364. [[CrossRef](#)]
35. Li, Z.; Ding, S.; Kong, L.; Wang, X.; Ashour, A.; Han, B.; Ou, J. Nano TiO₂-engineered anti-corrosion concrete for sewage system. *J. Clean. Prod.* **2022**, *337*, 130508. [[CrossRef](#)]
36. Kumar, A.M.; Khan, A.; Hussein, M.A.; Khan, M.Y.; Dafalla, H.; Suresh, B.; Ramakrishna, S. Hybrid nanocomposite coatings from PEDOT and BN-TiO₂ nanosheets: Enhanced invitro corrosion resistance, wettability and biocompatibility for biomedical applications. *Prog. Org. Coat.* **2022**, *170*, 106946. [[CrossRef](#)]

37. Zhang, Y.; Zhang, K.; Lei, S.; Su, Y.; Yang, W.; Wang, J.; Qin, G.; Li, W. Formation and oxidation behavior of TiO₂ modified Al₂O₃-Nb₂O₅/NbAl₃ composite coating prepared by two-step methods. *Surf. Coat. Technol.* **2022**, *433*, 128081. [[CrossRef](#)]
38. Devikala, S.; Kamaraj, P.; Arthanareeswari, M. Corrosion resistance behavior of PVA/TiO₂ composite in 3.5% NaCl. *Mater. Today Proc.* **2018**, *5*, 8672–8677. [[CrossRef](#)]
39. Rostami, S.; Mahdavi, S.; Alinezhadfar, M.; Mohseni, A. Tribological and corrosion behavior of electrochemically deposited Co/TiO₂ micro/nano-composite coatings. *Surf. Coat. Technol.* **2021**, *423*, 127591. [[CrossRef](#)]
40. Anwar, S.; Khan, F.; Zhang, Y. Corrosion behaviour of Zn-Ni alloy and Zn-Ni-nano-TiO₂ composite coatings electrodeposited from ammonium citrate baths. *Process. Saf. Environ. Prot.* **2020**, *141*, 366–379. [[CrossRef](#)]
41. Wang, K.; Wang, J.; Fan, J.; Lotya, M.; O'Neill, A.; Fox, D.; Feng, Y.; Zhang, X.; Jiang, B.; Zhao, Q.; et al. Ultrafast saturable absorption of two-dimensional MoS₂ nanosheets. *ACS Nano* **2013**, *7*, 9260–9267. [[CrossRef](#)]
42. Asan, G.; Asan, A.; Çelikkan, H. The effect of 2D-MoS₂ doped polypyrrole coatings on brass corrosion. *J. Mol. Struct.* **2020**, *1203*, 127318. [[CrossRef](#)]
43. Xia, Y.; He, Y.; Chen, C.; Wu, Y.; Chen, J. MoS₂ nanosheets modified SiO₂ to enhance the anticorrosive and mechanical performance of epoxy coating. *Prog. Org. Coat.* **2019**, *132*, 316–327. [[CrossRef](#)]
44. Hu, S.; Muhammad, M.; Wang, M.; Ma, R.; Du, A.; Fan, Y.; Cao, X.; Zhao, X. Corrosion resistance performance of nano-MoS₂-containing zinc phosphate coating on Q235 steel. *Mater. Lett.* **2020**, *265*, 127256. [[CrossRef](#)]
45. Chen, C.; He, Y.; Xiao, G.; Xia, Y.; Li, H.; He, Z. Two-dimensional hybrid materials: MoS₂-RGO nanocomposites enhanced the barrier properties of epoxy coating. *Appl. Surf. Sci.* **2018**, *444*, 511–521. [[CrossRef](#)]
46. Sasaki, T.; Kooli, F.; Iida, M.; Michiue, Y.; Takenouchi, S.; Yajima, Y.; Izumi, F.; Chakoumakos, B.C.; Watanabe, M. A Mixed Alkali Metal Titanate with the Lepidocrocite-like Layered Structure. Preparation, Crystal Structure, Protonic Form, and Acid–Base Intercalation Properties. *Chem. Mater.* **1998**, *10*, 4123–4128. [[CrossRef](#)]
47. Zhang, Z.; Li, W.; Yuen, M.F.; Ng, T.-W.; Tang, Y.; Lee, C.-S.; Chen, X.; Zhang, W. Hierarchical composite structure of few-layers MoS₂ nanosheets supported by vertical graphene on carbon cloth for high-performance hydrogen evolution reaction. *Nano Energy* **2015**, *18*, 196–204. [[CrossRef](#)]
48. Singh, S.; Singh, G.; Bala, N. Corrosion behavior and characterization of HA/Fe₃O₄/CS composite coatings on AZ91 Mg alloy by electrophoretic deposition. *Mater. Chem. Phys.* **2019**, *237*, 121884. [[CrossRef](#)]
49. Hu, S.; Li, W.; Finklea, H.; Liu, X. A review of electrophoretic deposition of metal oxides and its application in solid oxide fuel cells. *Adv. Colloid Interface Sci.* **2020**, *276*, 102102. [[CrossRef](#)] [[PubMed](#)]
50. Hoshide, T.; Zheng, Y.; Hou, J.; Wang, Z.; Li, Q.; Zhao, Z.; Ma, R.; Sasaki, T.; Geng, F. Flexible Lithium-Ion Fiber Battery by the Regular Stacking of Two-Dimensional Titanium Oxide Nanosheets Hybridized with Reduced Graphene Oxide. *Nano Lett.* **2017**, *17*, 3543–3549. [[CrossRef](#)]
51. Maluangnont, T.; Matsuba, K.; Geng, F.; Ma, R.; Yamauchi, Y.; Sasaki, T. Osmotic Swelling of Layered Compounds as a Route to Producing High-Quality Two-Dimensional Materials. A Comparative Study of Tetramethylammonium versus Tetrabutylammonium Cation in a Lepidocrocite-type Titanate. *Chem. Mater.* **2013**, *25*, 3137–3146. [[CrossRef](#)]
52. Peng, F.; Zhang, D.; Liu, X.; Zhang, Y. Recent progress in superhydrophobic coating on Mg alloys: A general review. *J. Magnes. Alloy.* **2021**, *9*, 1471–1486. [[CrossRef](#)]
53. Zhang, M.; Xu, H.; Zeze, A.L.P.; Liu, X.; Tao, M. Coating performance, durability and anti-corrosion mechanism of organic modified geopolymer composite for marine concrete protection. *Cem. Concr. Compos.* **2022**, *129*, 104495. [[CrossRef](#)]
54. Gong, C.; Jianzhong, L.; Cuicui, C.; Changfeng, L.; Liang, S. Study on silane impregnation for protection of high performance concrete. *Procedia Eng.* **2012**, *27*, 301–307. [[CrossRef](#)]
55. Wang, S.; Wang, Y.; Zou, Y.; Wu, Y.; Chen, G.; Ouyang, J.; Jia, D.; Zhou, Y. A self-adjusting PTFE/TiO₂ hydrophobic double-layer coating for corrosion resistance and electrical insulation. *Chem. Eng. J.* **2020**, *402*, 126116. [[CrossRef](#)]
56. Parichehr, R.; Dehghanian, C.; Nikbakht, A. Preparation of PEO/silane composite coating on AZ31 magnesium alloy and investigation of its properties. *J. Alloys Compd.* **2021**, *876*, 159995. [[CrossRef](#)]
57. Wu, C.; Liu, Q.; Chen, R.; Liu, J.; Zhang, H.; Li, R.; Takahashi, K.; Liu, P.; Wang, J. Fabrication of ZIF-8@SiO₂ Micro/Nano Hierarchical Superhydrophobic Surface on AZ31 Magnesium Alloy with Impressive Corrosion Resistance and Abrasion Resistance. *ACS Appl. Mater. Interfaces* **2017**, *9*, 11106–11115. [[CrossRef](#)]
58. Zhang, G.; Qin, S.; Yan, L.; Zhang, X. Simultaneous improvement of electromagnetic shielding effectiveness and corrosion resistance in magnesium alloys by electropulsing. *Mater. Charact.* **2021**, *174*, 111042. [[CrossRef](#)]
59. Liu, H.; Tong, Z.; Zhou, W.; Yang, Y.; Jiao, J.; Ren, X. Improving electrochemical corrosion properties of AZ31 magnesium alloy via phosphate conversion with laser shock peening pretreatment. *J. Alloys Compd.* **2020**, *846*, 155837. [[CrossRef](#)]